



Microscale optoelectronic infrared-to-visible upconversion devices and their use as injectable light sources

He Ding^{a,1}, Lihui Lu^{b,c,1}, Zhao Shi^a, Dan Wang^d, Lizhu Li^a, Xichen Li^e, Yuqi Ren^b, Changbo Liu^a, Dali Cheng^a, Hoyeon Kim^f, Noel C. Giebink^f, Xiaohui Wang^g, Lan Yin^d, Lingyun Zhao^d, Minmin Luo^{b,c}, and Xing Sheng^{a,2}

^aDepartment of Electronic Engineering, Beijing National Research Center for Information Science and Technology, Tsinghua University, 100084 Beijing, China; ^bNational Institute of Biological Sciences, 102206 Beijing, China; ^cSchool of Life Sciences, Tsinghua University, 100084 Beijing, China; ^dSchool of Materials Science and Engineering, Tsinghua University, 100084 Beijing, China; ^eDepartment of Electrical and Computer Engineering, University of Texas at Austin, Austin, TX 78712; ^fDepartment of Electrical Engineering, The Pennsylvania State University, University Park, PA 16802; and ^gTianjin Zhonghuan Neolight Technology Co., Ltd., 120111 Tianjin, China

Edited by John A. Rogers, Northwestern University, Evanston, IL, and approved May 16, 2018 (received for review February 5, 2018)

Optical upconversion that converts infrared light into visible light is of significant interest for broad applications in biomedicine, imaging, and displays. Conventional upconversion materials rely on nonlinear light-matter interactions, exhibit incidence-dependent efficiencies, and require high-power excitation. We report an infrared-to-visible upconversion strategy based on fully integrated microscale optoelectronic devices. These thin-film, ultraminiaturized devices realize near-infrared (~810 nm) to visible [630 nm (red) or 590 nm (yellow)] upconversion that is linearly dependent on incoherent, low-power excitation, with a quantum yield of ~1.5%. Additional features of this upconversion design include broadband absorption, wide-emission spectral tunability, and fast dynamics. Encapsulated, free-standing devices are transferred onto heterogeneous substrates and show desirable biocompatibilities within biological fluids and tissues. These microscale devices are implanted in behaving animals, with in vitro and in vivo experiments demonstrating their utility for optogenetic neuromodulation. This approach provides a versatile route to achieve upconversion throughout the entire visible spectral range at lower power and higher efficiency than has previously been possible.

upconversion | optoelectronics | optogenetics

The photon upconversion process converts multiple low-energy photons into a higher energy photon via so-called anti-Stokes emission (1–4), gathering enormous interest in many applications, including biological imaging (5–7), solar energy harvesting (8–11), infrared (IR) sensing (12, 13), displays (14), and solid-state cooling (15). In particular, designed upconversion materials and structures with capabilities of converting IR photons within the “biological transparency window” (~800–1,000 nm) to visible ones are of critical importance to deep-tissue light delivery for biomedical diagnosis and treatment (16–19). State-of-the-art upconversion techniques commonly rely on anti-Stokes mechanisms, including two-photon absorption, second-harmonic generation, and other transition schemes like excited-state absorption and energy transfer upconversion (3, 4, 20–23). However, such processes are typically nonlinear and require coherent or high excitation power (typically laser sources), exhibiting narrow-band and polychromatic excitations and emissions, low and illumination-dependent efficiencies (0.001~1%), and slow responses (μ s to ms) (4). Recently reported upconversion materials based on triplet-triplet annihilation present relatively high quantum yields (>1%), but these materials are usually susceptible to oxygen and render small anti-Stokes shifts (22, 23). An alternative upconversion approach involves physically connected or bonded photodetectors and light-emitting devices, with external circuits or power sources to compensate the energy difference and obtain high gains (12, 13, 24). Such device schemes provide viable solutions to IR imaging;

however, bulky chips and circuits create challenges for further miniaturization.

In this article, we present materials and device concepts to overcome these issues, by exploiting thin-film, ultracompact, optoelectronic upconversion devices based on semiconductor heterostructures. Through photon–“free electron”–photon processes, such concepts eliminate the constraints of conventional nonlinear upconversion approaches. Fabricated microscale devices realize self-powered IR-to-visible upconversion, with a linear response (quantum yield >1%) under incoherent low-power excitation (as low as 10 mW/cm²). Additionally, the upconverting devices exhibit monochromatic emission [630 nm (red) or 590 nm (yellow)], broadband sensitivity (400–900 nm), and fast transient decays (lifetime, 47 ns). Integrated with biocompatible encapsulates and substrates, these upconversion devices can be implanted into subdermal tissues and demonstrate both in vitro and in vivo light delivery and neural interrogation.

Significance

Materials and devices that upconvert photons from low to high frequencies are of tremendous interest for broad applications in bio- and chemical sensing, infrared imaging, display, and photovoltaics. Here we develop self-powered, micrometer-scale optoelectronic upconversion devices for infrared-to-visible photon upconversion. The realized microscale optoelectronic device exhibits a practical efficiency of 1.5% under incoherent low-power illumination, with emission intensity linearly dependent on excitation. Other remarkable advances over conventional approaches include broadband absorption, wide-emission spectral tunability (red, yellow, and blue), and fast dynamics. Encapsulated ultraminiaturized devices can be implanted into subdermal tissues and provide stable operation in behaving animals. Demonstrations of optogenetic stimulation in living animals present their potential for biomedical uses.

Author contributions: H.D., L.Y., L.Z., M.L., and X.S. designed research; H.D., L. Lu, Z.S., D.W., L. Li, X.L., Y.R., C.L., D.C., H.K., N.C.G., X.W., and X.S. performed research; X.S. developed the concepts and performed theoretical analysis; H.D., Z.S., L. Li, X.L., C.L., H.K., N.C.G., X.W. and X.S. performed material and device design, fabrication, and characterization; H.D., D.C., and X.S. performed the simulations; H.D., L. Lu, Z.S., D.W., Y.R., L.Y., L.Z., M.L. and X.S. designed and performed biological experiments; H.D., L. Lu, and X.S. analyzed data; and H.D. and X.S. wrote the paper in consultation with the other authors.

The authors declare no conflict of interest.

This article is a PNAS Direct Submission.

Published under the PNAS license.

¹H.D. and L. Lu contributed equally to this work.

²To whom correspondence should be addressed. Email: xingsheng@tsinghua.edu.cn.

This article contains supporting information online at www.pnas.org/lookup/suppl/doi:10.1073/pnas.1802064115/-DCSupplemental.

Published online June 11, 2018.

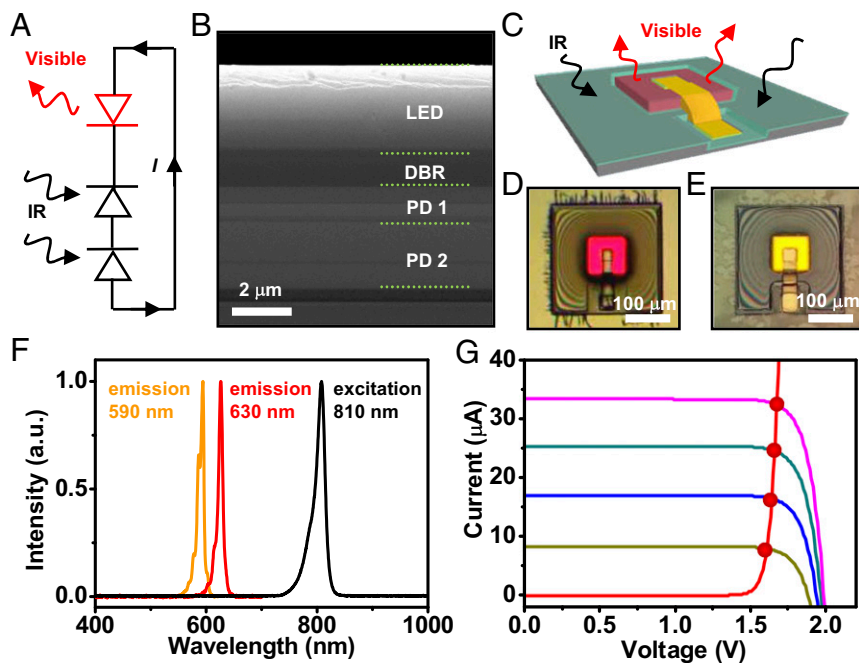


Fig. 1. Schematic illustrations and images of microscale IR-to-visible upconversion devices and their optoelectronic properties. (A) The operational principle of the upconversion device design, in which serially connected photodiodes absorb IR light to drive a visible LED. (B) SEM image (cross-sectional view) of the epitaxial multilayer stack composed of one layer of a GaInP or AlGaInP LED, one layer of a DBR, and one layer for a GaAs DJPD on a GaAs substrate. (C) Schematic illustration of the fabricated upconversion device (tilted view), with the patterned LED (red color) and DJPD (gray color) connected by the deposited metal contact (yellow color) and encapsulated by SU-8 (green color). (D and E) Microscopic image (top view) of representative upconversion devices with red (D) and yellow (E) emissions under IR excitation. (F) Emission spectra of the excitation source (an 810-nm IR LED), the IR-to-red and the IR-to-yellow upconversion devices with peaks at 630 nm and 590 nm, respectively. (G) Current–voltage curves of the two components in the upconversion device: the GaInP red LED (red curve) and the GaAs DJPD under IR illumination with various power densities (21, 43, 60, and 79 mW/cm²). DBR, distributed Bragg reflector.

Results

Demonstration of Microscale, IR-to-Visible Upconversion Devices. Fig. 1A schematically illustrates our proposed upconversion strategy based on fully integrated microscale optoelectronic devices. Here photovoltaic diodes (PDs) capture low-energy IR photons, providing photogenerated currents and voltages that drive a light-emitting diode (LED) to emit high-energy visible photons. Since a single IR PD made by low-bandgap semiconductors cannot supply enough photovoltage to turn on the visible LED, two or more PDs are serially connected to compensate the voltage difference and retain energy conservation for IR-to-visible upconversion. Detailed balance analysis suggests that such a combined “photon-to-electron” and “electron-to-photon” process is able to approach the thermodynamic limits of photon energy conversion (*SI Appendix, Figs. S1 and S2*). Fig. 1B depicts a cross-sectional SEM image of the designed device structure, which is based on a serially connected double junction (DJ) gallium arsenide (GaAs) PD (bandgap ~ 1.4 eV) and an aluminum gallium indium phosphide (AlGaInP)-based visible LED, which can be Ga_{0.5}In_{0.5}P for red emission (bandgap ~ 1.9 eV) or Al_{0.15}Ga_{0.35}In_{0.5}P for yellow emission (bandgap ~ 2.1 eV) (more details in *SI Appendix, Fig. S3 and Table S1*). Each junction in the GaAs DJPD is designed to realize current matching and maximum operating efficiency at ~ 810 nm, with a thin-film GaAs tunnel junction in between. The top AlGaInP LED is connected to the GaAs PDs by a conductive AlInP/AlGaInP-based distributed Bragg reflector for improved efficiency at corresponding (red or yellow) emission wavelengths (*SI Appendix, Fig. S4*). Formed by metal organic chemical vapor deposition, the multilayered device stack (~ 9 - μm thick) is lattice

matched and epitaxially grown on a GaAs substrate with an Al_{0.95}Ga_{0.05}As-based sacrificial layer that can be selectively eliminated later for thin-film device release. Followed by lithographic etching and deposition processes (*SI Appendix and SI Appendix, Fig. S5*), the top p-type gallium phosphide layer of the AlGaInP LED and the bottom p-GaAs layer of the GaAs PD are connected by metalized contacts (Fig. 1C).

The finalized upconversion device has lateral dimensions of $220 \times 220 \mu\text{m}^2$ and an active layer thickness of $9 \mu\text{m}$, emitting red light at ~ 630 nm (Fig. 1D) or yellow light at ~ 590 nm (Fig. 1E) under incoherent illumination provided by an IR LED at ~ 810 nm with a power density as low as 2 mW/cm^2 , showing anti-Stokes shifts of 0.4 and 0.6 eV for IR-to-red and IR-to-yellow upconversions, respectively (Fig. 1F). Unlike typical rare-earth-based upconverting materials with polychromatic emissive spectra (5, 9), the light output from our upconversion devices is purely monochromatic and widely tunable based on semiconductor compositions, which is advantageous for applications like chemical sensing (25). Dependent on the semiconductor bandgap, the other spectral shifts (e.g., near-IR to blue upconversion) can be realized by applying similar device integration schemes with suitable semiconductor emitting devices (*SI Appendix, Figs. S8 and S9*). Current and voltage characteristics are measured from the GaInP red LED and the GaAs DJPD under different illumination powers (Fig. 1G). The results indicate that both the LED and the DJPD work under their optimal operating voltages (1.6–1.8 V) across a wide range of excitation powers. Large arrays of such upconversion devices ($>100 \times 100$ devices) are formed with high fabrication yields ($>99\%$) on a 2-inch GaAs

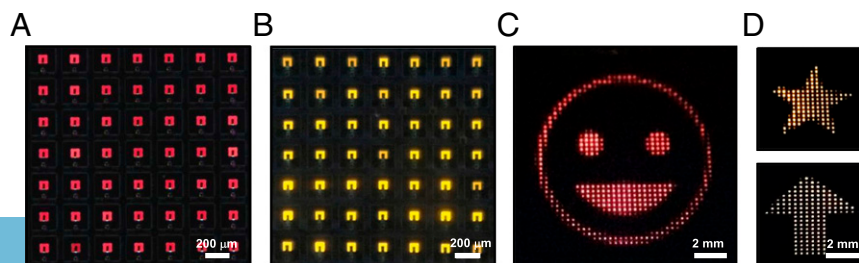


Fig. 2. Optical images of microscale IR-to-visible upconversion device arrays. (A and B) Optical image of fabricated IR-to-red (A) and IR-to-yellow (B) upconversion device arrays under 810-nm IR illumination. (C and D) Photographs of representative images captured with a red (C) emission upconversion device array and a yellow (D) emission upconversion device array under patterned IR illuminations.

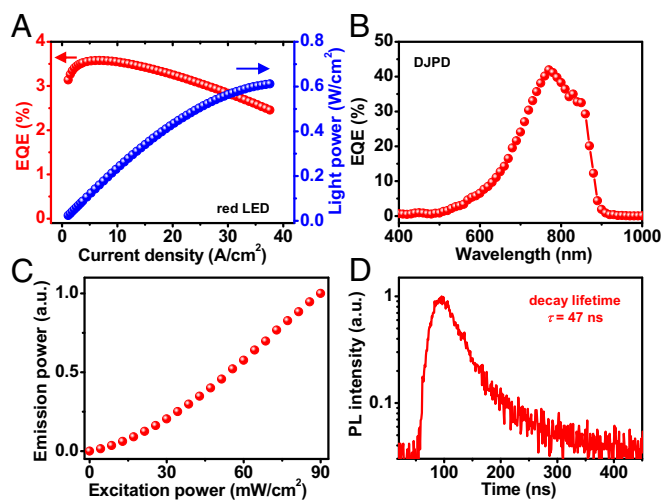


Fig. 3. Measured performance of the IR-to-red upconversion device. (A) EQE (red curve) and light output power density (blue curve) as a function of current density for the GaInP red LED. (B) EQE spectrum of the GaAs DJPD. (C) Emission power as a function of the excitation light (at 810 nm) density for the integrated upconversion device. (D) Photoluminescence decay of the integrated upconversion device. PL, photoluminescence.

substrate. Representative photographs of IR-to-red and IR-to-yellow upconversion device arrays are shown in Fig. 2 *A* and *B*, respectively. Fig. 2 *C* and *D* (with more examples in *SI Appendix, Fig. S10*) presents multiple captured red-emitting and yellow-emitting images by passing collimated light from an 810-nm LED through different patterned transparency masks, demonstrating direct IR-to-visible imaging capabilities.

Performance of Upconversion Devices. Fig. 3 further characterizes the detailed performance measured from our designed upconversion device structures. Independent thin-film GaInP red LED and GaAs DJPD (with details provided in *SI Appendix, Tables S2 and S3*) devices with the same designs as those in the integrated heterostructure (Fig. 1*B* and *SI Appendix, Table S1*) are fabricated separately on GaAs substrates and released onto polyimide substrates by transfer printing (26, 27). Fig. 3*A* plots the measured external quantum efficiency (EQE) and output light power vs. current density for a GaInP red LED with a size of $80 \times 80 \mu\text{m}^2$. The EQE peaks at 3.6% under an input current density of $\sim 5 \text{ A/cm}^2$ and decreases at higher currents, probably as a result of heating. The EQE of GaInP LEDs is mainly limited by

the inefficient light extraction associated with high refractive indices ($n = 3.5$) of III–V materials, with an estimated extraction efficiency of $1/2n^2 = 3.9\%$ (28). The fact that the calculated extraction efficiency is very close to the experimental EQE suggests that the epi-grown GaInP LED has a near-unity ($>90\%$) internal quantum yield. The AlGaInP yellow LEDs with similar structures present relatively lower EQE than the red ones due to the increased Al composition in the active emitting layers (29). Fig. 3*B* shows the measured EQE spectra for the GaAs DJPD under normal incidence, while EQE spectra of the two separate subcells are provided in *SI Appendix, Fig. S6*. The GaAs DJPD exhibits a wide excitation range from 600 to 900 nm, with a maximum EQE reaching 42% at $\sim 770 \text{ nm}$, where the top and bottom GaAs cells are current matched. The deviation from the theoretical limit (50% for the two-photon process) is mainly associated with the reflection loss at the nonoptimized III–V/air interface. With the growth substrate removed, photon response by backside illumination is also observed (*SI Appendix, Fig. S6*). The excitation spectra in our upconversion devices can be tuned by selecting appropriate semiconductors. Combining the red LED and the DJPD, the fabricated upconversion device reaches a practical IR-to-visible conversion efficiency of 1.5% under normal incidence. Separately measured results for the red LED and DJPD indicate that very high ($>90\%$) internal electron–photon conversion efficiencies are realized for these high-quality III–V-based devices, and the external quantum efficiencies are mostly limited by the nonideal optical absorption and extraction. Implemented with optimal optical designs for the LED and the DJPD (30–32), the upconversion efficiency of the integrated device can be further improved and approach the thermodynamic limit (50% for the two-photon process) without theoretical constraints (*SI Appendix* and *SI Appendix, Figs. S1 and S2*).

The fully formed IR-to-red upconversion device is excited by an incoherent, low-power IR LED bulb ($\sim 810 \text{ nm}$), with its emission spectra captured by a fiber-coupled spectrometer. The integrated emission intensity (from 610 to 650 nm) vs. incident IR power density is plotted in Fig. 3*C*. We can clearly see that the emission is linearly dependent on the excitation incidence at a power as low as 10 mW/cm^2 , in comparison with one-sun illumination (100 mW/cm^2). This is because both high-performance LEDs and detectors can operate linearly under low-injection currents or illumination. At lower excitation power ($<10 \text{ mW/cm}^2$), the sublinear behavior is mainly attributed to the low LED efficiency associated with nonradiative recombination at low currents. By contrast, upconversion processes based on traditional nonlinear energy transfer mechanisms exhibit much lower efficiencies ($\sim 0.01\%$) at such low-incident powers and require much higher irradiance (typically $>1 \text{ W/cm}^2$) to reach linear operation and saturated efficiencies ($\sim 2\%$) (4, 33). The impulse response of

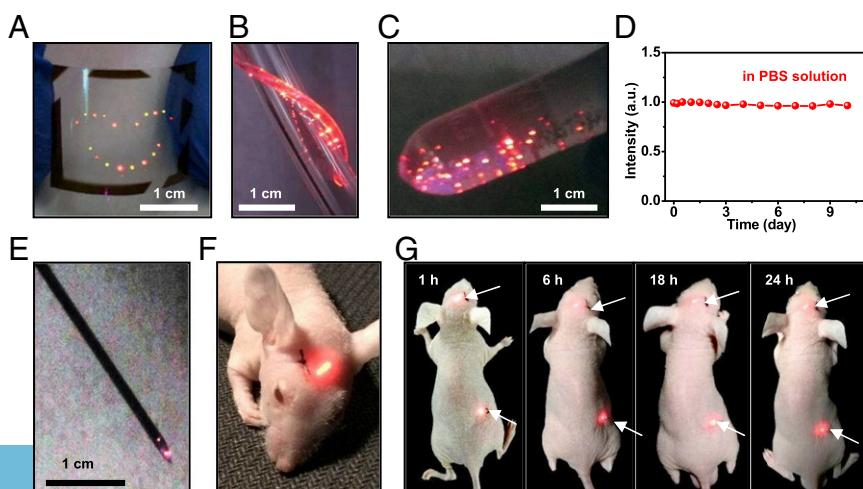


Fig. 4. Released thin-film microscale upconversion devices integrated with various systems. (A) An array of devices transferred onto a flexible PET film under uniform IR illumination. (B) A collection of devices integrated with a stretchable PDMS fiber with guided IR light, wrapped onto a plastic cylindrical tube. (C) A collection of released devices dispersed in PBS. (D) The luminance stability of encapsulated devices for different immersion times in PBS. (E) Microscale devices injected from a syringe needle. (F) Image of a nude mouse with devices implanted s.c. (G) Photos showing the luminance stability of the implanted devices within 24 h. PDMS, polydimethylsiloxane; PET, polyethylene terephthalate.

the upconverted photoluminescence following a 30-ns excitation pulse (780-nm laser) is shown in Fig. 3D and *SI Appendix*, Fig. S14. Measured elapsed time for the increase in the upconversion luminescence in response to the excitation pulse is ~ 10 ns, and the initial decay exhibits an exponential lifetime of 47 ns, which is due primarily to the resistive-capacitive time constant of the circuit. These results indicate that our upconversion devices show a fast response superior to previously reported materials and devices (7, 13, 21). To summarize, the fabricated microscale device presents highly efficient IR-to-visible upconversion with broadband sensitivity, linear responsivity, and fast response (*SI Appendix*, Table S5).

Freestanding Upconversion Devices on Heterogeneous Substrates.

The microscale, thin-film upconversion devices are released from the GaAs growth substrate by selectively removing the $\text{Al}_{0.95}\text{Ga}_{0.05}\text{As}$ sacrificial layer in hydrofluoric acids (34). The resulted free-standing devices ($\sim 9\text{-}\mu\text{m}$ thick) can be deterministically integrated with various heterogeneous substrates via transfer printing (34, 35). Fig. 4A and B, respectively, illustrates arrays of microscale devices on flexible polyethylene terephthalate and stretchable polydimethylsiloxane substrates, with more examples included in *SI Appendix*, Figs. S11 and S12. These passive, remotely IR-powered, visible-emitting devices are operated without external power sources or interconnect circuits; thus, denser and larger device arrays can be easily obtained at high yields. Behaving like microparticles, the fully released and encapsulated upconversion devices can be suspended in solutions, transported in microfluidic tubes, and ejected via syringe needles (Fig. 4C and E, *SI Appendix*, and *Movies S1* and *S2*). After encapsulation, a large collection of such thin-film devices are dispersed in aqueous solutions and retain their upconversion functionality for >10 d without degradation (Fig. 4C and D).

Biocompatibility Evaluation. Further in vitro and in vivo experiments were conducted to demonstrate potential uses of these upconversion devices in biology. Microscale devices were implanted into different subdermal regions of mice and rats (*SI Appendix*, Figs. S15–S18) with the approval of the Animal Care and Use Committee of Tsinghua University and the National Institute of Biological Sciences, Beijing. External IR light sources (810 nm) were remotely delivered into the subdermal tissue (in the head and the upper back), driving the devices to emit red light (630 nm) in freely behaving animals (Fig. 4F and G, *SI Appendix*, Fig. S17, and *Movie S3*). Such IR-to-red upconversion is important for efficient visible-light delivery in biological systems, since many substances in the tissue exhibit significant absorption in the visible range. For example, the extinction coefficient of hemoglobin at 630 nm is almost one order of magnitude larger than that at 810 nm (16). To assess the in vivo biocompatibility of the encapsulated upconversion devices, histological examinations of biopsied tissue samples around the implants as well as hematological evaluations of the Sprague–Dawley rats and C57 black 6 (C57BL/6N) mice were made. After 1–3 wk of implantation, no significant inflammatory reactions were observed (*SI Appendix*, Figs. S15, S16, and S18) and the implanted devices retained their

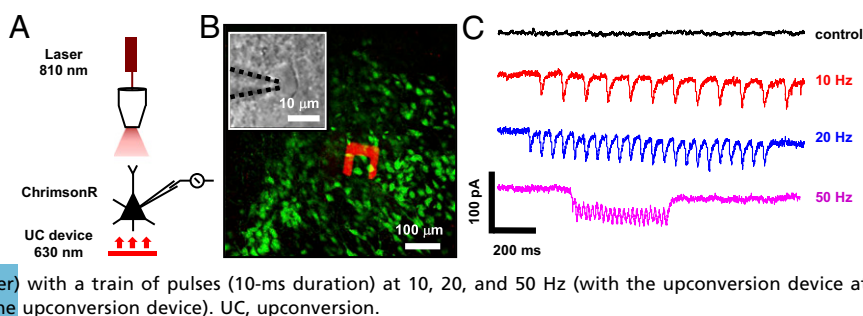
upconversion capabilities for up to 3 wk (*SI Appendix*, Figs. S15 and S17). From the representative views of H&E staining of the skin section adjacent to the devices at 1–3 wk after implantation (*SI Appendix*, Figs. S15 and S18), the eosinophilic infiltration was graded as minimal according to the number and distribution of eosinophils within the tissues surrounding the implants (36). In all, these results demonstrate the biocompatibility of the encapsulated upconversion devices as well as their chronic operation stability in biological systems.

In Vitro and In Vivo Neural Signal Interrogation. These self-powered, miniaturized IR-to-visible upconversion light sources provide unique opportunities for optogenetic stimulations by combining with genetically encoded optical actuators (37). Unlike other light delivery tools based on fiber-tethered light sources or wirelessly controlled LEDs driven by inductive coils, photovoltaic cells, or batteries (38–40), micro- and nanoscale upconverting materials and systems allows for minimally invasive s.c. implantation with visible light output by remotely delivered IR power. Despite successful demonstrations of optogenetic neuromodulation, conventional rare-earth-based upconverting materials (41–43) suffer from required high-power IR illumination ($>1\text{ W/mm}^2$) and slow responses. Our ultracompact (volume, $\sim 3 \times 10^{-4}\text{ mm}^3$; weight, $\sim 1\text{ }\mu\text{g}$) upconversion device overcomes the challenges of the above approaches with stable, efficient, and fast IR-to-visible upconversion.

The feasibility of this concept was first explored via in vitro experiments as shown in Fig. 5. While opsins sensitive to blue and green light are commonly utilized for optogenetics, red-shifted opsins sensitive to amber and red light are also of particular interest for independent control of distinct neuron populations (44). Here, microscale upconversion devices were placed underneath cultured brain slices ($\sim 200\text{-}\mu\text{m}$ thick) with neural cells expressing ChrimsonR (produced by Shanghai Taitool Bioscience, Co. Ltd) and illuminated with a near-IR laser (810 nm) (Fig. 5A). IR illumination penetrates into the brain tissue and excites red emission (630 nm) that interrogates ChrimsonR-expressing neurons, with intracellular signals recorded by a perforated whole-cell patch-clamp setup (Fig. 5B). Under IR illumination (810 nm) with an OD of 15 mW/mm^2 , the power density of upconverted red emission (630 nm) on the device surface is estimated to be $\sim 1.1\text{ mW/mm}^2$ (see *Methods*), above the threshold ($\sim 1\text{ mW/mm}^2$) to activate ChrimsonR (44). Photocurrents of a patch-clamped cell above the red-emitting device were recorded under pulsed illumination (duration of 10 ms, 810 nm) with various frequencies (10, 20, and 50 Hz), and the corresponding continuous bursts of spiking response are shown in Fig. 5C. In addition, cells responses were examined without the upconversion device underneath, suggesting that direct IR illumination cannot activate ChrimsonR-expressing neurons, which is consistent with the literature (44).

To further demonstrate the in vivo applicability, the synchronization of neural activities with upconversion devices was examined in the optogenetics experiment. IR-to-red upconversion devices were transferred onto polyimide-based flexible probe substrates and implanted into the mouse brain (*SI Appendix*, Fig. S19). As excitatory neurons in the primary somatosensory cortex

Fig. 5. In vitro optogenetic neural modulation using a microscale upconversion device. (A) Schematic illustration of the setup to measure intracellular signals of ChrimsonR-expressing nerves under IR illumination. (B) Confocal fluorescence image of an upconversion device (red color) underneath cultured neural cells expressing ChrimsonR-EGFP (green color). The *Inset* shows a whole-cell patch-clamp pipette (black dashed lines) that records photocurrent signals from a neuron. (C) A series of photocurrent signals recorded from a ChrimsonR-expressing neuron under IR illumination (810-nm laser) with a train of pulses (10-ms duration) at 10, 20, and 50 Hz (with the upconversion device at the *Bottom*), as well as the control results (without the



(S1) show strong synchronization under light activation with low frequencies (45), the local field potential (LFP) can be measured in the S1 to analyze synchronous local network activities. To specifically label excitatory neurons in the S1, ChrimsonR is expressed in the S1 of calcium/calmodulin dependent protein kinase II alpha (Camk2a)-Cre knock-in mice (Fig. 6 A and B). To evaluate the caused injury or neuroinflammatory response of implantation, the astrocyte activation and microglia accumulation in the S1 were estimated within various times (Fig. 6C and *SI Appendix, Fig. S20*). The implanted region exhibited normal immunological effects, and immunoreactive glial responses were similar to those results based on optical fiber probes, flexible devices and fluorescent nanoparticles (38–41). In this invasive operation, the tissue lesion was mainly attributed to the probe substrate and encapsulation layers, and it could be further minimized using cellular-scale device structures (*SI Appendix, Fig. S21*) and other advanced thin-film coating techniques (46). In vivo recordings of LFP in the S1 were performed under transcranial IR irradiation (810 nm) in conscious Camk2a-Cre mice, where the upconversion device probe

is facing the ChrimsonR-expressing region and under IR illumination (*SI Appendix, Fig. S19*). Pulsed stimulation at 8 Hz with upconverted light (630 nm) induced an increased LFP power at the same frequency (Fig. 6 D–F), indicating that such periodic optical activations generate theta oscillations in the cortical region (45). Control groups without ChrimsonR expression, absence of upconversion devices probe, or only IR light were performed and all showed no significant LFP power increase (Fig. 6 D–F), suggesting the upconversion devices could effectively emit red light to manipulate the activated ChrimsonR-expressing neurons. Taken together, these results establish the utility of our microscale upconversion devices as implantable light sources for wireless optogenetic control of in vitro and in vivo neuroactivities.

Discussion

In conclusion, concepts presented here demonstrate materials and device strategies for highly efficient IR-to-visible upconversion that bypass many limitations of previously explored

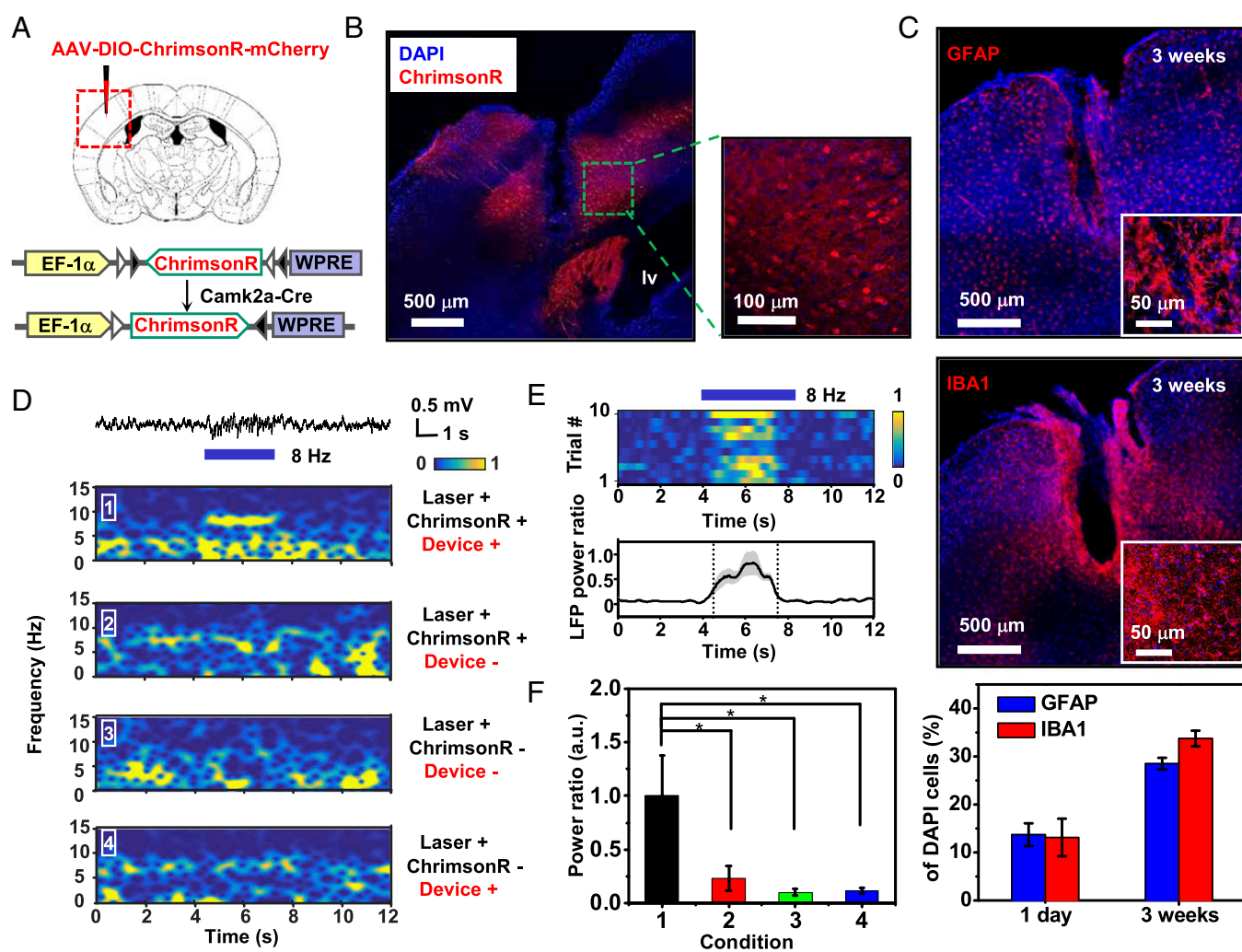


Fig. 6. In vivo optogenetic stimulation with upconversion devices. (A) The strategy of labeling of Camk2a neurons with ChrimsonR by injecting AAV-DIO-ChrimsonR-mCherry-WPRE vectors into the primary somatosensory cortex (S1) of Camk2a-Cre mice. (B) Images of ChrimsonR-mCherry (red) expression in S1. (C) Images of S1 regions after 3 wk of implantation, respectively stained for GFAP+ astrocytes (Top) or IBA1+ microglia (Middle), and percentages of the cell population indicated by DAPI cells (Bottom) ($n = 3$ mice for each group). (D) LFP recording in response to 8-Hz IR stimulation (810 nm, 10-ms pulses, 3-s duration) of S1 under different conditions. (E) The effects of IR stimulation. (Top) Heatmaps draw power at 8 Hz of individual trials. (Bottom) Average of normalized power at 8 Hz. (F) Normalized power ratio of the light activation under the corresponding conditions of D ($n = 3$ mice, 10 trials per mouse). * $P < 0.05$, t test. AAV, adeno-associated virus; DIO, double-floxed inverted open reading frame; IBA1, ionized calcium-binding adapter molecule 1; WPRE, woodchuck hepatitis virus posttranscriptional regulatory element.

techniques. Considering that epi-grown inorganic semiconductor devices (LEDs, solar cells, etc.) have already realized very high internal energy conversion efficiencies (30, 32), it was observed that the upconversion efficiency of our current device design is mainly constrained by the low LED extraction efficiency. Advanced surface treatments and optical coatings, such as textures and photonic crystals (31, 35, 47), can immediately lead to higher upconversion efficiencies. In addition, it will be highly desirable to further scale down the device geometry to cellular scale ($<10\ \mu\text{m}$) and even molecular scale ($<100\ \text{nm}$), and advanced bottom-up and top-down fabrication approaches (48, 49) can be utilized to achieve device structures with much smaller footprints. Such micro- and nanostructured geometries are not only advantageous for improved biointegration but also can significantly mitigate the light confinement by approaching the subwavelength scales (50), ultimately reaching thermodynamic limits (*SI Appendix*). Some preliminary explorations were performed to achieve a device structure with a dimension of $<10\ \mu\text{m}$, similar to the size of neurons (*SI Appendix*, Fig. S21).

The involvement of other semiconductors, like gallium nitrides, silicon, and indium arsenide, could be used to explore excitation and emission at other wavelengths, enabling versatile sensing and displaying capabilities. Besides direct epi-growth, approaches like wafer bonding and transfer printing can be explored to realize highly compact, heterogeneously integrated structures. In particular, it would be highly desirable to develop devices upconverting IR to blue and green colors (with preliminary work shown in *SI Appendix*, Fig. S9). By combining with light-sensitive receptors or drugs (51), these miniaturized devices can be applied to deep-tissue light stimulation or therapy. These results provide routes for high-performance upconversion materials and devices and their unprecedented potential as optical biointerfaces.

ACKNOWLEDGMENTS. We thank C. Z. Ning, Y. Huang, Y. Luo, and Z. Hao (Tsinghua University) for their help in experiments and valuable discussions. The research is supported by National Natural Science Foundation of China Grants 51602172 (to X.S.) and 51601103 (to L.Y.) and 1000 Youth Talents Program in China (to L.Y. and X.S.).

- Raman CV (1928) A new radiation. *Indian J Phys* 2:387–398.
- Auzel F (2004) Upconversion and anti-stokes processes with f and d ions in solids. *Chem Rev* 104:139–173.
- Zhou B, Shi B, Jin D, Liu X (2015) Controlling upconversion nanocrystals for emerging applications. *Nat Nanotechnol* 10:924–936.
- Zhang F (2015) *Photon Upconversion Nanomaterials* (Springer, Berlin).
- Wang F, et al. (2011) Tuning upconversion through energy migration in core-shell nanoparticles. *Nat Mater* 10:968–973.
- Lay A, et al. (2017) Upconverting nanoparticles as optical sensors of nano- to micro-Newton forces. *Nano Lett* 17:4172–4177.
- Liu Y, et al. (2017) Amplified stimulated emission in upconversion nanoparticles for super-resolution nanoscopy. *Nature* 543:229–233.
- Trupke T, Shalav A, Richards BS, Wurfel P, Green MA (2006) Efficiency enhancement of solar cells by luminescent up-conversion of sunlight. *Sol Energy Mater Sol Cells* 90:3327–3338.
- Zou WQ, Visser C, Maduro JA, Pshenichnikov MS, Hummelen JC (2012) Broadband dye-sensitized upconversion of near-infrared light. *Nat Photonics* 6:560–564.
- Briggs JA, Atre AC, Dionne JA (2013) Narrow-bandwidth solar upconversion: Case studies of existing systems and generalized fundamental limits. *J Appl Phys* 113:124509.
- Green MA, Bremner SP (2016) Energy conversion approaches and materials for high-efficiency photovoltaics. *Nat Mater* 16:23–34.
- Yang Y, Zhang YH, Shen WZ, Liu HC (2011) Semiconductor infrared up-conversion devices. *Prog Quant Electron* 35:77–108.
- Yu H, et al. (2016) High-gain infrared-to-visible upconversion light-emitting phototransistors. *Nat Photon* 10:129–134.
- Downing E, Hesselink L, Ralston J, Macfarlane R (1996) A three-color, solid-state, three-dimensional display. *Science* 273:1185–1189.
- Ha S-T, Shen C, Zhang J, Xiong Q (2016) Laser cooling of organic-inorganic lead halide perovskites. *Nat Photon* 10:115–121.
- Weissleder R (2001) A clearer vision for in vivo imaging. *Nat Biotechnol* 19:316–317.
- Idris NM, et al. (2012) In vivo photodynamic therapy using upconversion nanoparticles as remote-controlled nanotransducers. *Nat Med* 18:1580–1585.
- Mura S, Nicolas J, Couvreur P (2013) Stimuli-responsive nanocarriers for drug delivery. *Nat Mater* 12:991–1003.
- Yang D, et al. (2015) Current advances in lanthanide ion (Ln(3+))-based upconversion nanomaterials for drug delivery. *Chem Soc Rev* 44:1416–1448.
- Aouani H, Rahmani M, Navarro-Cia M, Maier SA (2014) Third-harmonic-upconversion enhancement from a single semiconductor nanoparticle coupled to a plasmonic antenna. *Nat Nanotechnol* 9:290–294.
- Wang J, et al. (2014) Enhancing multiphoton upconversion through energy clustering at sublattice level. *Nat Mater* 13:157–162.
- Ye C, Zhou L, Wang X, Liang Z (2016) Photon upconversion: From two-photon absorption (TPA) to triplet-triplet annihilation (TTA). *Phys Chem Chem Phys* 18:10818–10835.
- Wu MF, et al. (2016) Solid-state infrared-to-visible upconversion sensitized by colloidal nanocrystals. *Nat Photon* 10:31–34.
- Zhao L, Thompson P, Faleev N, Prather D, Appelbaum I (2007) Two-photon passive electro-optic upconversion in a GaAs/AlGaAs heterostructure device. *Appl Phys Lett* 90:121132.
- Wong HT, Chan HL, Hao J (2010) Towards pure near-infrared to near-infrared upconversion of multifunctional GdF(3):Yb(3+),Tm(3+) nanoparticles. *Opt Express* 18:6123–6130.
- Meitl MA, et al. (2006) Transfer printing by kinetic control of adhesion to an elastomeric stamp. *Nat Mater* 5:33–38.
- Park SI, et al. (2009) Printed assemblies of inorganic light-emitting diodes for deformable and semitransparent displays. *Science* 325:977–981.
- Schubert EF (2006) *Light-Emitting Diodes* (Cambridge Univ Press, New York).
- Lee JW, et al. (2016) An elegant route to overcome fundamentally-limited light extraction in AlGaN deep-ultraviolet light-emitting diodes: Preferential outcoupling of strong in-plane emission. *Sci Rep* 6:22537.
- Schnitzer I, Yablonovitch E, Caneau C, Gmitter TJ (1993) Ultrahigh spontaneous emission quantum efficiency, 99.7-percent internally and 72-percent externally, from AlGaAs/GaAs/AlGaAs double heterostructures. *Appl Phys Lett* 62:131–133.
- Wierer JJ, David A, Megens MM (2009) III-nitride photonic-crystal light-emitting diodes with high extraction efficiency. *Nat Photon* 3:163–169.
- Green MA, et al. (2017) Solar cell efficiency tables (version 50). *Prog Photovolt Res Appl* 25:668–676.
- Page RH, et al. (1998) Upconversion-pumped luminescence efficiency of rare-earth-doped hosts sensitized with trivalent ytterbium. *J Opt Soc Am B* 15:996–1008.
- Yoon J, et al. (2010) GaAs photovoltaics and optoelectronics using releasable multilayer epitaxial assemblies. *Nature* 465:329–333.
- Sheng X, et al. (2014) Printing-based assembly of quadruple-junction four-terminal microscale solar cells and their use in high-efficiency modules. *Nat Mater* 13:593–598.
- Macleod TM, Williams G, Sanders R, Green CJ (2005) Histological evaluation of Permacol as a subcutaneous implant over a 20-week period in the rat model. *Br J Plast Surg* 58:518–532.
- Deisseroth K (2011) Optogenetics. *Nat Methods* 8:26–29.
- Kim TJ, et al. (2013) Injectable, cellular-scale optoelectronics with applications for wireless optogenetics. *Science* 340:211–216.
- Park SI, et al. (2015) Soft, stretchable, fully implantable miniaturized optoelectronic systems for wireless optogenetics. *Nat Biotechnol* 33:1280–1286.
- Park SI, et al. (2015) Ultraminaturized photovoltaic and radio frequency powered optoelectronic systems for wireless optogenetics. *J Neural Eng* 12:056002–56002.
- Chen S, et al. (2018) Near-infrared deep brain stimulation via upconversion nanoparticle-mediated optogenetics. *Science* 359:679–684.
- Hososhima S, et al. (2015) Near-infrared (NIR) up-conversion optogenetics. *Sci Rep* 5:16533.
- Huang K, Dou QQ, Loh XJ (2016) Nanomaterial mediated optogenetics: Opportunities and challenges. *RSC Adv* 6:60896–60906.
- Klapoetke NC, et al. (2014) Independent optical excitation of distinct neural populations. *Nat Methods* 11:338–346.
- Cardin JA, et al. (2009) Driving fast-spiking cells induces gamma rhythm and controls sensory responses. *Nature* 459:663–667.
- Fang H, et al. (2016) Ultrathin, transferred layers of thermally grown silicon dioxide as biofluid barriers for biointegrated flexible electronic systems. *Proc Natl Acad Sci USA* 113:11682–11687.
- Sheng X, et al. (2011) Design and fabrication of high-index-contrast self-assembled texture for light extraction enhancement in LEDs. *Opt Express* 19:A701–A709.
- Huang Y, Duan X, Lieber CM (2005) Nanowires for integrated multicolor nanophotonics. *Small* 1:142–147.
- Hobbs RG, Petkov N, Holmes JD (2012) Semiconductor nanowire fabrication by bottom-up and top-down paradigms. *Chem Mater* 24:1975–1991.
- Yan RX, Gargas D, Yang PD (2009) Nanowire photonics. *Nat Photon* 3:569–576.
- Yun SH, Kwok SJJ (2017) Light in diagnosis, therapy and surgery. *Nat Biomed Eng* 1:0008 (2017).